A&A, 710, L10 (2026)
https://doi.org/10.1051/0004-6361/202659553

Astronomy & Astrophysics

LETTER TO THE EDITOR

Hourly radio variability of PDS 70c from time-differential photometry

Simon Casassus[1,2,⋆], Miguel Cárcamo[3,2], Oriana Domínguez-Jamett[1], Yuhiko Aoyama[4], Gabriel-Dominique Marleau[5,6], Ondřej Chrenko[7], Hauyu Baobab Liu[8], and Barbara Ercolano[9]

[1] Departamento de Astronomía, Universidad de Chile, Casilla 36-D Santiago, Chile
[2] Data Observatory Foundation, Eliodoro Yáñez 2990, Providencia, Santiago, Chile
[3] University of Santiago of Chile (USACH), Faculty of Engineering, Computer Engineering Department, Santiago, Chile
[4] School of Physics and Astronomy, Sun Yat-sen University, Guangdong 519082, People's Republic of China
[5] Fakultät für Physik, Universität Duisburg-Essen, Lotharstraße 1, 47057 Duisburg, Germany
[6] Max-Planck-Institut für Astronomie, Königstuhl 17, 69117 Heidelberg, Germany
[7] Charles University, Faculty of Math and Physics, Astronomical Institute, V Holešovičkách 747/2, 180 00 Prague 8, Czech Republic
[8] Department of Physics, National Sun Yat-Sen University, No. 70, Lien-Hai Road, Kaohsiung City 80424, Taiwan
[9] University Observatory, Faculty of Physics, Ludwig-Maximilians-Universität München, Scheinerstr. 1, 81679 Munich, Germany

Received 21 February 2026 / Accepted 18 April 2026

ABSTRACT

Context. The radio emission mechanisms from accreting protoplanets and their variability link observations and physical properties.
Aims. We revisit the variability of the ~343 GHz (ALMA Band 7) flux density from PDS 70c (F_{B7}).
Methods. The subtraction of the extended time-averaged signal may enable the measurement of the flux density from variable and embedded point sources. Visibility alignment and self-calibration yield close to thermal residuals in each execution block (EB) of ALMA observations, thus allowing the time-differential photometry of point-sources in the visibility domain. The variability of PDS 70c was checked against synthetic control point sources.
Results. In images of the 2017 ALMA dataset, with three ~1 h EBs, PDS 70c was detected only on 6 December 2017, where F_{B7} rose by 228% ± 69% (3.3σ). Time-differential photometry confirms a rise by 170% ± 46% (3.7σ). An application to ~2 h EBs from the 2023 dataset resulted in constant flux densities, within a scatter of ~15%. However, $F_{B7}(t)$ shows some scatter when splitting the deep 2023 EBs into 20 min intervals, with a χ^2 test significant at 2.6σ, and an intrinsic dispersion of 49% ± 21%.
Conclusions. The radio variability of PDS 70c, observed over hours but averaged out on longer timescales, is indeed expected if the signal is due to H I free-free from an accretion shock on a circumplanetary disk surface. A planet-to-environment mass ratio $<10^{-4}$ is required to avoid smoothing by radiative diffusion if the signal is due to thermal emission from the environment.

Key words. planets and satellites: formation – protoplanetary disks – submillimeter: planetary systems – stars: individual: PDS 70 – techniques: interferometric

1. Introduction

Most embedded protoplanet candidates known to date, such as PDS 70b,c, AB Aur b, WISPIT 2b, and 2MASS J16120668-3010270 b, are Hα sources and thought to be undergoing mass accretion (Keppler et al. 2018; Haffert et al. 2019; Wang et al. 2021; Christiaens et al. 2024; Hammond et al. 2025; Currie et al. 2025; van Capelleveen et al. 2025; Li et al. 2025; Close et al. 2025b). Among these candidates, only PDS 70c is known to have a radio counterpart (Isella et al. 2019; Benisty et al. 2021; Fasano et al. 2025; Domínguez-Jamett et al. 2025). The sub-millimetre continuum signal from PDS 70c is particularly important as it constrains the planetary accretion rate and conditions in its environment, provided the radio emission mechanisms are understood. By contrast, Hα observations (Zhou et al. 2025; Close et al. 2025a) can be affected by variable extinction (Cugno et al. 2025).

Based on nearly-coeval multi-frequency ALMA measurements, Domínguez-Jamett et al. (2025) suggest that, contrary to the standard hypothesis, the sub-millimetre signal is probably not due to thermal dust emission, as its optically thick spectral index over 97 GHz, 145 GHz, and 343 GHz (Band 7, hereafter IB23) is difficult to reconcile with the partially thick emission from a circumplanetary disk or envelope. It may instead be due to thermal plasma radiation, either with residual ionisation, as in a cool star (i.e. due to the H^- or H_2^- free-free continua), or fully ionised, as in an H II region. A 671 GHz drop suggests that the most likely explanation for the signal from PDS 70c is H I free-free from a thin H II region at the shocked surface of a circumplanetary disk (CPD) undergoing mass loading (as described by Aoyama et al. 2018; Szulágyi & Ercolano 2020).

The spectral analysis of Domínguez-Jamett et al. (2025) rests on the hypothesis that variability is negligible, which is justified by the short time span encompassing the multi-frequency observations, of two months at most. Indeed, the IB23 dataset, acquired in nine execution blocks (EBs) spanning six months, suggests that the Band 7 flux density of PDS 70c (hereafter F_{B7}) is constant within a standard deviation of 10%. In fact, F_{B7} appears constant (Table 1) when comparing the discovery observation in the 2017 dataset (Isella et al. 2019), hereafter IB17 (following the nomenclature of Benisty et al. 2021), with measurements in 2019 (hereafter LB19, Benisty et al. 2021), in 2021 (Fasano et al. 2025), and in 2023 (i.e. in IB23, Domínguez-Jamett et al. 2025).

⋆ Corresponding author: simon@das.uchile.cl

Table 1. Summary of the datasets used here and previous measurements for $F_{\rm B7}$, the Band 7 flux density for PDS 70c.

	θ mas	$F_{\rm B7}$ μJy	Year
IB17[a]	∼60	106 ± 19[a]	2017
LB19[b]	∼50	118 ± 24[c]	2019
IB23[d]	∼60	121 ± 13[d]	2023

Notes. [(a)] Isella et al. (2019). [(b)] Benisty et al. (2021). [(c)] Casassus et al. (2023). [(d)] Domínguez-Jamett et al. (2025).

However, motivated by questions on the uncertainties in restored images and in the concatenation of observations, Casassus & Cárcamo (2022) and Casassus et al. (2023) chose PDS 70 as an example source to test an original scheme for multi-epoch visibility alignment (the `VisAlign` package) and to apply automatic self-calibration (with the `snow` package). Surprisingly, their revisit of IB17 yielded the non-detection of PDS 70c, despite sufficient signal-to-noise ratio (S/N) to reproduce the result of Isella et al. (2019). This non-detection led to the conclusion for variability of at least ∼40% over ∼2 yr.

We revised the analysis of Casassus & Cárcamo (2022) with the goal of resolving the discrepancy with all other measurements of $F_{\rm B7}$. It turns out that IB17 is composed of three EBs, dated 2, 3, and 6 December. However, perhaps as a result of a bug in the handling of `CASA` tasks (which we attribute to intensive calls to the `mstransform` task, combining both time and channel averaging), the EB from 6 December was missing. As shown below, the inclusion of 6 December brings $F_{\rm B7}$ into agreement with the original report by Isella et al. (2019). The variability reported by Casassus & Cárcamo (2022) therefore applies to timescales of days or less, rather than years.

Here, we report on a technique to estimate the flux density of unresolved yet variable embedded sources, and apply it to ALMA Band 7 datasets of PDS 70 (Sect. 2, the datasets are summarised in Table 1). We then discuss the expected timescales of the radio variability of PDS 70c for relevant emission mechanisms (Sect. 3). We conclude for a tentative detection of hourly variability, which favours an accretion shock at the CPD surface as the origin of the signal (Sect. 4).

2. Analysis and results

2.1. Individual EB imaging of IB17

Details on the alignment and self-calibration procedure are given in Appendix A. Imaging of the whole IB17 dataset (Fig. 1d, restored with Briggs parameter $r = 0.3$) confirms the detection of PDS 70c by Isella et al. (2019). Its flux density, given by the peak intensity at the position of the point source in restored maps, is $\langle F_{\rm B7}\rangle = 172 \pm 30\,\mu$Jy, where the average represents a joint measurement over all three EBs. As detailed in Appendix A alternative measurements with Gaussian fits yield similar values within the errors (Table A.1). We note that $\langle F_{\rm B7}\rangle$ is consistent at 1.8σ with the value reported by Isella et al. (2019).

However, imaging of individual EBs, shown in Fig. 1, revealed no signal under PDS 70c on 2 and 3 December. Since the source is known to exist, rather than assigning zero flux density, we recorded the specific intensity at the expected position (Table A.1). This strategy for point-source photometry incorporates prior knowledge of the source position (as discussed by Domínguez-Jamett et al. 2025, their Sect. 2.3), and is sometimes referred to as 'forced photometry' (Samland et al. 2017).

The source is, however, quite conspicuous on 6 December, at 370 ± 65 μJy or ∼5.7σ (as given by the peak specific intensity). The $F_{\rm B7}$ measurement on 6 December is roughly twice the average value of $\langle F_{\rm B7}\rangle$, and the difference between 3 and 6 December is 276±82.6 μJy and significant at 3.3σ. Fixing the average value of $F_{\rm B7}$ as given by Domínguez-Jamett et al. (2025, Table 1), this rise corresponds to 228% ± 69%.

2.2. Time-differential photometry

The preceding estimates for $F_{\rm B7}$ are, for simplicity, directly read out as the peak intensity under PDS 70c in restored images, where the source is separated from surrounding signal. But this approach requires artificially more weight in the longer baselines, overriding error propagation at the expense of sensitivity. In other words, with natural weights, the uncertainties would be lower, but the source would no longer be isolated from the outer ring (Fig. 1), thus introducing systematic errors.

We also tested the time variable nature of the radio signal from PDS 70c by measuring the relative variations in $F_{\rm B7}$ in the *uv* plane. Our method was to fit a point source fixed at the location of PDS 70c ($\boldsymbol{x}_\circ$, which was obtained with an elliptical Gaussian fit in 6 December), in the visibility residuals V^R after subtraction of the model visibilities calculated from the model image that best fits the concatenated dataset. Least-squares minimisation yields (notation follows from Casassus & Cárcamo 2022)

$$F_\nu = \frac{\sum_{l=1}^{L} \omega_l\, \Re\left[V_l^R e^{-2\pi i \boldsymbol{u}_l\cdot\boldsymbol{x}_\circ}\right]}{\mathcal{A}(\boldsymbol{x}_\circ)\sum_{l=1}^{L}\omega_l}, \tag{1}$$

where $\boldsymbol{u}_l$ is the *uv*-plane position for datum V_l^R and $\mathcal{A}(\boldsymbol{x}_\circ)$ is the primary-beam attenuation. The associated errors are

$$\sigma(F_\nu) = \frac{1}{\mathcal{A}(\boldsymbol{x}_\circ)\sqrt{\sum_{l=1}^{L}\omega_l}}. \tag{2}$$

A similar measurement of $F_{\rm B7}$ can also be obtained from the gridded visibilities. As shown in Appendix C, the gridded approach bypasses the model image, but it collapses the spectral information and depends on the gridding scheme. Since the model image is used in the self-calibration procedure anyways, we opted for photometric extraction on the raw data. Both approaches yield similar results for a flat spectral index (Fig. B.1).

Such time-differential photometry is deceivingly simple as it assumes perfect calibration. Any imperfection yields non-thermal residuals. For instance, omitting EB alignment with `VisAlign`, or omitting the amplitude self-calibration, yields such residuals, as documented in Appendix B and Fig. B.1. However, alignment and self-calibration allow reaching close to thermal residuals, even in natural weights.

Another difficulty in differential photometry is that the uncertainties $\sigma(F_\nu)$ derive from the visibility weights (Eq. (2)), whose absolute calibration is uncertain. This can be overcome with the replacement of the original weights by the root-mean-square dispersion of each visibility datum taken over all individual integrations, as is performed with the `CASA` task `statwt`. An additional imaging run is in order after the application of `statwt`, to check that it did not appreciably deteriorate the dynamic range.

A complementary method to estimate the uncertainty on *uv*-plane point-source photometry is to take statistics on flux densities extracted at randomly distributed positions. We refer

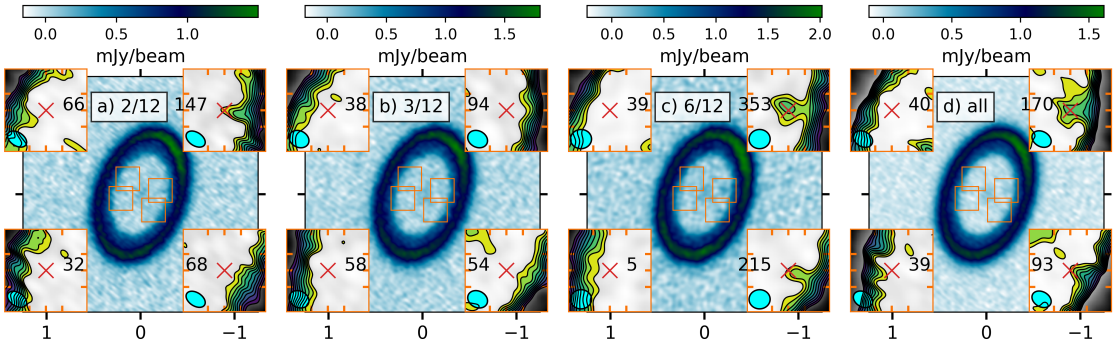

Fig. 1. Restored images for IB17. The insets zoom in on PDS 70c (to the north-east), and symmetric positions along disk axes. The image noise and beams are provided in Table A.1. Peak intensities are all equal when brought to a common beam.

to this estimate as the 'spatial scatter'. At a given epoch, we applied Eq. (1) at $N = 120$ random positions, and took the dispersion of the resulting N flux densities as a measure of its uncertainty. In the presence of an extended and strong signal, this uncertainty depends on position since imperfect antenna gains are multiplicative. Given that the source under consideration is roughly a ring, we chose to place the random positions along a projected circular orbit matching that of PDS 70c (but excluding the position of PDS 70c within one natural-weight beam).

The close to thermal residuals justify the use of Eq. (1) to extract point-source flux densities in the visibility residuals, and measure $\Delta F_{\rm B7}(t) = F_{\rm B7}(t) - \langle F_{\rm B7}\rangle$. The result is summarised in Fig. 2, where $F_{\rm B7}$ is consistent between 2 and 3 December, but rises by $206 \pm 56\,\mu$Jy from 3 to 6 December, which is significant at 3.7σ. Fixing $F_{\rm B7}$ to the value for IB23 in Table 1, this rise corresponds to 170% ± 46%. The quoted errors were derived from the spatial scatter, and they are very close to the errors given by the visibility weights (after the application of `statwt`).

As a test on the significance of the variability of PDS 70c, we injected three synthetic and constant point sources in the concatenated dataset at symmetric positions from PDS 70c relative to the disk minor and major axis. These positions match the centres of the insets in Fig. 1. Using the uncertainties inferred from the spatial scatter, as for PDS 70c, the largest variation in $\Delta F_{\rm B7}(t)$ for the synthetic point sources is $122 \pm 56\,\mu$Jy or 2.2σ.

An application of differential photometry to other Band 7 datasets is documented in Appendix D. Neither LB19 nor IB23 present detectable variability among EBs.

It is intriguing that the daily variability of $F_{\rm B7}$ is picked up in IB17, but not in IB23. The deep IB23 dataset spanned six months in nine EBs with integrations of over 2 h, while the IB17 EBs are 1 h long. Yet a search for variability, using a related approach to the time-differential photometry presented here (but subtracting a Gaussian fit to PDS 70c in the model image, so the source stands out in the residuals), yielded a constant value for $F_{\rm B7}$, with a scatter of ∼10% among EBs (Domínguez-Jamett et al. 2025). Perhaps the source underwent a peculiar glitch right on 6 December. However, given that the IB23 EBs are more than twice as long in IB17, an interesting possibility is that the variability of PDS 70c occurs on timescales of minutes or hours rather than days, and that it is averaged out in longer integrations.

The difficulty in observing fine-grained time variability is that splitting into shorter integrations results in noisier measurements. As documented in Appendix D, we nonetheless picked up some scatter in $\Delta F_{\rm B7}(t)$ in ∼20 min intervals of the IB23 dataset, corresponding to a reduced χ^2 of 1.7 with 41 degrees of freedom,

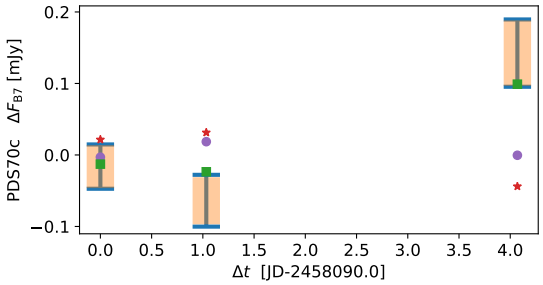

Fig. 2. Time-differential photometry of PDS 70c. The blue $\pm 1\sigma$ error bars (2σ in total) record $\Delta F_{\rm B7} = F_{\rm B7} - \langle F_{\rm B7}\rangle$ as a function of Julian day for each EB. The same quantity extracted from the spatial scatter (see text) is shown with thick orange error bars. Each type of marker corresponds to three synthetic and constant point sources injected at the positions of the insets in Fig. 1.

or significant at $2.6\,\sigma$. The intrinsic rms variability of PDS 70c is $\sigma_{\rm int} = 59 \pm 25\,\mu$Jy.

3. Discussion

The constraints on the radio variability of PDS 70c bring information on the emission mechanisms in the circumplanetary environment. For example, radiative heating from accretion bursts could provide external forcing to the emitting medium. The radio variability would result from the intrinsic variability of accretion smoothed by the timescale associated with thermal diffusion.

The interpretation that $F_{\rm B7}$ stems from an accretion shock at a CPD surface around PDS 70c (Domínguez-Jamett et al. 2025) naturally accounts for fast variability. Since the accretion flows within the Hill sphere can be approximated as free fall (e.g. Tanigawa et al. 2012; Fung & Chiang 2016), the free-free emission responds directly to fluctuation in the inflow from the protoplanetary disk, that can vary by factors of a few along the planetary orbit in turbulent disks (Gressel et al. 2013) or for eccentric planets (Li et al. 2023). However, in their hydro-dynamical models of the CPD surface shock, Takasao et al. (2021) find that the interaction between the infalling gas and the CPD triggers high-frequency and stochastic variability through thermal instability of the standing shock. The net mass accretion rate on the CPD surface, and eventually on the protoplanet itself, result from the interaction of post-shock cooling and flow dynamics in the CPD. This accretion rate fluctuates by up to an order of magnitude on timescales much shorter than the orbital period, and down to hours. By contrast, accretion occurs on a quasi-steady state if averaged over days, as in the proposal of Sect. 2.2 to explain the lack of detectable variability on longer timescales.

In the case of a surface shock, the H I free-free emission reflects the temperature profile across the shock (Aoyama et al. 2018). From the shock profiles shown in Domínguez-Jamett et al. (2025) for two representative pre-shock conditions, in the region where $\tau(300\,\mathrm{GHz}) \sim 1$ and $T \sim 3\times10^4$ K to 3×10^5 K, at depths of $\sim10^4$ cm and $\sim10^5$ cm, respectively. Given that the main source of opacity is optically thin, except at radio frequencies, energy transfer occurs over a light-crossing time, which is essentially instantaneous.

Alternatively, the radio signal may stem from the bulk mass in the planetary environment under external forcing. Assuming energy transfer in an optically thick medium via Rosseland diffusion, the typical photon mean-free-path is $l_R = 1/(\kappa_R\,\rho)$, where κ_R is the Rosseland opacity and ρ is the mass density. The diffusion timescale is $\tau_d = N_{\rm scat}\,l_R/c$, with $N_{\rm scat} = (L/l_R)^2$, and where L is the typical size of the emitting region.

We distributed the mass in the planetary environment $M_{\rm env}$, in a cubic box with side L, representing the linear size of a CPD or of an envelope. The outer radius of the CPD could be a third of the Hill radius, or ∼1 au for PDS 70c, and a typical aspect ratio is ∼0.1, so $L \sim 0.1$ au. Then the diffusion timescale is $\tau_d = M_{\rm env}\,\kappa_R/(c\,L)$. Reducing the box side, or increasing κ_R, results in larger diffusion timescales for a given mass.

The floor κ_R in a dust-deprived medium, with residual ionisation, is due to the H^- or H_2^- free-free continua and to atomic or molecular lines (e.g. Malygin et al. 2014). In a CPD accounting for the PDS 70c radio spectrum (Domínguez-Jamett et al. 2025), the annulus with the peak contribution to the net flux density, at $R = 0.05$ au, has a mid-plane $\rho \sim 10^{-8}$ g cm^{-3} and $T \sim 2000$ K, and $\kappa_{\rm R} \gtrsim 0.1$ (for solar metallicity, Malygin et al. 2014, their Fig. 3). The contribution from dust can hardly exceed this floor value, at least for large dust grains which have $\kappa_R \sim 0.1$ cm^2 g^{-1} for a standard gas-to-dust mass ratio of 100 (e.g. Chrenko et al. 2025).

An environment mass of $M_{\rm env} \sim 0.07\,M_{\rm Jup}$ for a planet-to-CPD mass ratio of 10^{-2} (considering a planet mass of $7\,M_{\rm Jup}$, Wang et al. 2021) is, in practice, an upper limit. The corresponding dust mass of $0.2\,M_\oplus$ is larger than the total mass of the Galilean moons, which is $0.07\,M_\oplus$. It is also much larger than the dust mass inferred from modelling $F_{\rm B7}$ assuming thermal dust emission, or $\sim1.4\times10^{-2}\,M_\oplus$ (Shibaike & Mordasini 2024).

If $M_{\rm env} = 0.07\,M_{\rm Jup}$, if $L = 0.1$ au, and if $\kappa_R = 0.1$ cm^2 g^{-1}, then $\tau_d = 3.5$ d. Fixing $\tau_d = 1$ h would require a box with a side of $L = \kappa_R \times M_{\rm env}/(c \times \tau_d) \sim 8$ au, which is much larger than the constraint of $L < 1$ au (from the limit on the angular extent of the source). Alternatively, the environment mass would have to be reduced to $M_{\rm env} = 8\times10^{-4}\,M_{\rm Jup}$ to match an hourly variability.

4. Conclusions

Imaging individual (∼1 h) EBs in the 2017 Band 7 observations of PDS 70 shows that PDS 70c is conspicuous on 6 December 2017, but undetectable on both 2 and 3 December. Estimates of the flux density from PDS 70c in the restored images ($F_{\rm B7}$) result in a rise from 3 to 6 December, which is significant at 3.3σ.

Time-differential photometry allows the extraction of the relative variations of $F_{\rm B7}$ in the *uv* plane, at a higher significance than in the restored images, where the source is confused with the outer ring. The residual Band 7 flux density of PDS 70c ($\Delta F_{\rm B7}$, after subtraction of the time-averaged extended emission) also rose from 3 to 6 December, by 3.7σ. Since the residuals in single EBs are not perfectly thermal, this estimate is tentative.

Tests on the variability of PDS 70c in Band 7 observations from 2023, with EBs twice as long than in 2017, yield a limit of ∼15%, as given by the dispersion of $\Delta F_{\rm B7}$ among seven EBs, which is consistent with a constant. However, splitting these 2 h EBs in 20 min intervals results in some intrinsic variability, significant at 2.6σ, and with an intrinsic rms scatter of 59 ± 25 μJy. These results tentatively suggest that the radio signal from PDS 70c is variable by ∼50% ± 21% on timescales of hours, but that its variability is averaged out on longer timescales.

As shown recently, existing models of surface accretion onto a CPD account for the PDS 70c radio spectrum (Domínguez-Jamett et al. 2025). Such models also predict high-frequency and stochastic planetary accretion variability, on timescales of hours, and averaged to a steady state on longer timescales (Takasao et al. 2021). If the radio signal stems from the surface shock itself, then the observed radio variability directly follows the accretion variability. In turn, if the radio signal stems from bulk mass in the planetary environment, then the environment mass must be at least a factor $\sim10^{-4}$ lower than the planetary mass to bring the diffusion timescale down to 1 h.

Acknowledgements. We thank the referee, Luis Peña-Moñino, for a constructive report, and also Myriam Benisty and Daniele Fasano for sharing their version of the IB17 dataset, which included Dec. 6. S.C. and M.C. acknowledge support from Agencia Nacional de Investigación y Desarrollo de Chile (ANID) given by FONDECYT Regular grant 1251456, and ANID project Data Observatory Foundation DO210001. G.-D.M. acknowledges the support of the Deutsche Forschungsgemeinschaft (DFG) through grant MA 9185/2-1. O.C. acknowledges the Czech Science Foundation (grant 25-16507S), the Charles University Research Centre program (No. UNCE/24/SCI/005), and the Ministry of Education, Youth and Sports through the e-INFRA CZ (ID:90254). This paper makes use of the following ALMA data: ADS/JAO.ALMA#2017.A.00006.S, ADS/JAO.ALMA#2018.A.00030.S, ADS/JAO.ALMA#2022.1.01477.S. ALMA is a partnership of ESO (representing its member states), NSF (USA) and NINS (Japan), together with NRC (Canada), NSTC and ASIAA (Taiwan), and KASI (Republic of Korea), in cooperation with the Republic of Chile. The Joint ALMA Observatory is operated by ESO, AUI/NRAO and NAOJ.

References

Aoyama, Y., Ikoma, M., & Tanigawa, T. 2018, ApJ, 866, 84
Benisty, M., Bae, J., Facchini, S., et al. 2021, ApJ, 916, L2
Cárcamo, M., Román, P. E., Casassus, S., Moral, V., & Rannou, F. R. 2018, Astron. Comput., 22, 16
Casassus, S., & Cárcamo, M. 2022, MNRAS, 513, 5790
Casassus, S., Cieza, L., Cárcamo, M., et al. 2023, MNRAS, 526, 1545
Chael, A. A., Johnson, M. D., Bouman, K. L., et al. 2018, ApJ, 857, 23
Chrenko, O., Casassus, S., & Chametla, R. O. 2025, A&A, 700, A82
Christiaens, V., Samland, M., Henning, T., et al. 2024, A&A, 685, L1
Close, L. M., Males, J. R., Li, J., et al. 2025a, AJ, 169, 35
Close, L. M., van Capelleveen, R. F., Weible, G., et al. 2025b, ApJ, 990, L9
Cugno, G., Facchini, S., Alarcon, F., et al. 2025, AJ, 170, 317
Currie, T., Hashimoto, J., Aoyama, Y., et al. 2025, ApJ, 990, L42
Domínguez-Jamett, O., Casassus, S., Baobab Liu, H., et al. 2025, A&A, 702, A18
Fasano, D., Benisty, M., Curone, P., et al. 2025, A&A, 699, A373
Fung, J., & Chiang, E. 2016, ApJ, 832, 105
Gressel, O., Nelson, R. P., Turner, N. J., & Ziegler, U. 2013, ApJ, 779, 59
Haffert, S. Y., Bohn, A. J., de Boer, J., et al. 2019, Nat. Astron., 3, 749
Hammond, I., Christiaens, V., Price, D. J., et al. 2025, MNRAS, 539, 1613
Isella, A., Benisty, M., Teague, R., et al. 2019, ApJ, 879, L25
Keppler, M., Benisty, M., Müller, A., et al. 2018, A&A, 617, A44
Li, Y.-P., Chen, Y.-X., & Lin, D. N. C. 2023, MNRAS, 526, 5346
Li, J., Close, L. M., Long, F., et al. 2025, ApJ, 990, L70
Malygin, M. G., Kuiper, R., Klahr, H., Dullemond, C. P., & Henning, T. 2014, A&A, 568, A91
Samland, M., Mollière, P., Bonnefoy, M., et al. 2017, A&A, 603, A57
Shibaike, Y., & Mordasini, C. 2024, A&A, 687, A166
Szulágyi, J., & Ercolano, B. 2020, ApJ, 902, 126
Takasao, S., Aoyama, Y., & Ikoma, M. 2021, ApJ, 921, 10
Tanigawa, T., Ohtsuki, K., & Machida, M. N. 2012, ApJ, 747, 47
van Capelleveen, R. F., Ginski, C., Kenworthy, M. A., et al. 2025, ApJ, 990, L8
Wang, J. J., Vigan, A., Lacour, S., et al. 2021, AJ, 161, 148
Zhou, Y., Bowler, B. P., Sanghi, A., et al. 2025, ApJ, 980, L39

Appendix A: Alignment, self-calibration and image-plane $F_{\rm B7}$ measurements in the IB17 dataset

Description of the IB17 ALMA dataset, alignment of EBs and imaging follow from Casassus & Cárcamo (2022), Casassus et al. (2023), and references therein. In brief, the 3 continuum spectral windows were time-averaged to 6.06 s, and binned into 8 channels. Individual EBs from 3 and 6 December 2017 were then aligned to the first EB, from 2 December, using the `VisAlign` package, including a correction for visibility amplitudes α_R. The resulting offsets were $\alpha_R = 1.102 \pm 0.002$, $\Delta\alpha = 0\farcs00845 \pm 0\farcs00034$, $\Delta\delta = -0.00045^{+0.0004}_{-0.00044}$, for 3 December, and $\alpha_R = 1.225 \pm 0.003$, $\Delta\alpha = 0\farcs0107 \pm 0\farcs0004$, $\Delta\delta = 0\farcs0043 \pm 0.0005$, for 6 December. An offset in flux scale of ∼20% is consistent with the nominal calibration uncertainty in ALMA Band 7, of ∼ 10% rms, while the positional offsets along R.A. and Dec. are all consistent with the nominal pointing accuracy, of ∼ 1/10 the naturally weighted beam of $0\farcs09 \times 0\farcs08$.

Following alignment, we concatenated the data into a single measurement set, and applied the `snow` package for automatic self calibration (`snow` replaces the tclean imager by `gpu-uvmem`, Cárcamo et al. 2018, in otherwise standard `CASA` self-calibration). Phase-only self-calibration did not yield improvements. However, a single iteration in amplitude and phase self-calibration, with a solution interval limited to a single scan (roughly 50 s), improved the peak S/N from 55 to 115.

Once self-calibrated, each EB was split for separate imaging with `gpu-uvmem`, in pure-χ^2 reconstructions (i.e. without entropy regularisation, but truncating the optimisation at ten iterations). The (non-parametric) model images were restored using Briggs weights with a robustness parameter $r = 0.3$. The resulting images are shown in Fig. 1.

Table A.1 provides a summary of the image properties in the IB17 dataset. We also tabulate the values of $F_{\rm B7}$ measured in each EB as well as in the concatenated dataset. The elliptical Gaussian fits were carried out following two strategies: 1- by fitting a beam, assuming that the source is unresolved, and 2- by fitting an elliptical Gaussian. Fitting a beam resulted in a bias for larger flux densities to account for extended low-level emission. Fitting an elliptical Gaussian was sensitive on the definition of the zoomed region around PDS 70c, and turned out to be impossible in the case of the concatenated dataset, where the source is connected to the ring.

Appendix B: Residual maps on single EBs and impact of alignment and self-calibration

Reaching thermal residuals in a dataset comprised of several EBs is routinely achieved, provided with sufficiently accurate calibration. However, because of the varying flux scale and pointing, the residuals under individual EBs will, in general, not be thermal. The application of both EB alignment (with `VisAlign`), along with amplitude and phase self-calibration, allowed reaching close to thermal residuals in the 2017 dataset, as illustrated in Fig. B.1. The omission of alignment or self-calibration leads to strong residuals, due to imperfect calibration of the visibility data.

Amplitude self-calibration of the IB17 dataset required short solution intervals, down to a single scan or 50 s. As a result, the derived antenna gains can be fairly noisy. We found the resulting gains vary strongly, up to ∼100% rms. These strongly variable gains modulate the point-source flux densities, in ways that cannot be corrected for with a single scaling factor (as with `VisAlign`). These noisy gains are probably at the origin of the persistent non-thermal residuals. Improvements in self-calibrations techniques, such as with 'closure imaging' (Chael et al. 2018), might allow purely thermal residuals in this dataset.

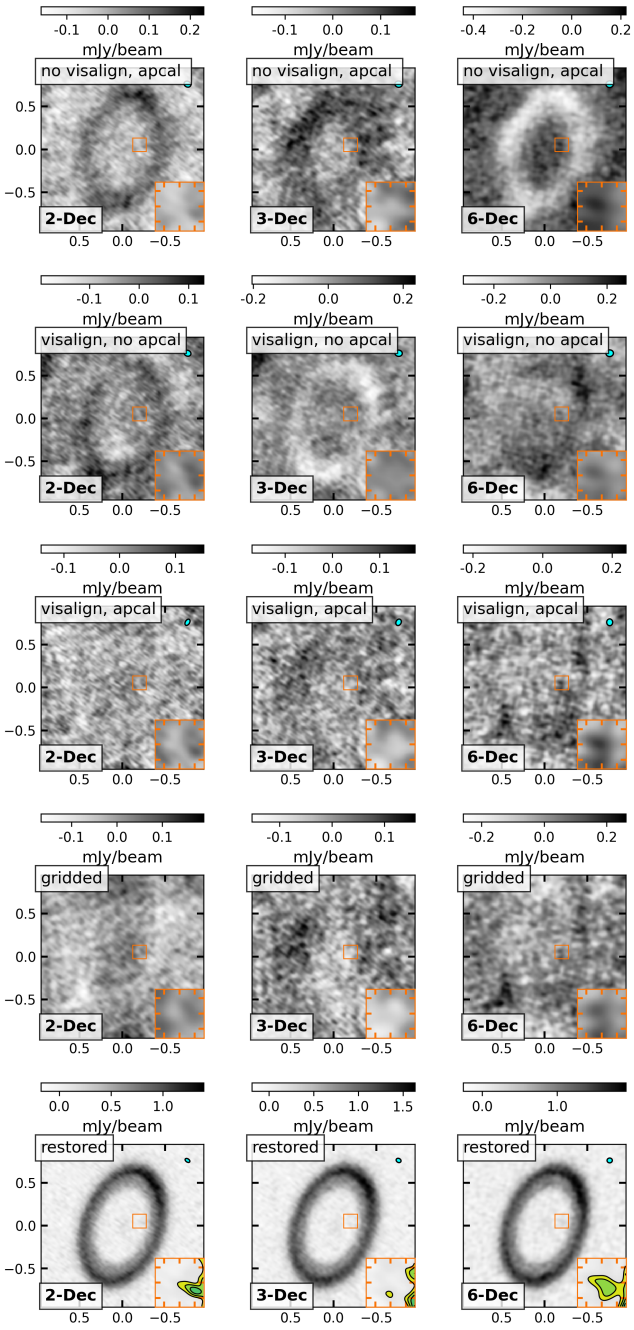

Fig. B.1. Dirty map residuals in natural weights for each EB, after subtraction of the model visibilities from the concatenated dataset. Insets zoom on PDS 70c, in the same colour stretch as for the image. Each row, from top to bottom, shows: 'no visalign, apcal', without `visalign` alignment, but after amplitude and phase self-calibration (apcal); 'visalign, no apcal': with alignment, but no self-calibration; 'visaligned, ap': here with both alignment and self-calibration, and reaching close to thermal residuals; 'gridded': also with both alignment and self-calibration, but from the gridded approach (i.e. $I_{\rm diff}$ in Eq. C.3); 'restored': restored maps, obtained with $r = 0.3$ (as in Fig. 1).

Table A.1. Summary of image properties and flux densities for PDS 70c (F_{B7}) in the IB17 dataset, as obtained in the sky images.

Date	Beam[(a)] mas	Noise[(b)] μJy	Peak[(c)] μJy	Beam fit[(d)] μJy	Gauss fit[(e)] μJy	Gauss fit[(e)] mas
2/12/2017	64×41	44	147 ± 44[(f)]	...	...	...
3/12/2017	63×50	51	94 ± 51[(f)]	...	...	...
6/12/2017	64×58	65	370 ± 65	502 ± 65	878 ± 210	$111^{+17}_{-10} \times 79^{+12}_{-12}$
All	62×46	30	172 ± 30	250 ± 30	...[(g)]	...[(g)]

Notes. [(a)] Elliptical Gaussian fit to the beam. [(b)] Standard dispersion of the residual images (i.e. 1σ noise). [(c)] F_{B7} from peak intensity under PDS 70c in restored maps. [(d)] F_{B7} from fitting the elliptical Gaussian clean beam. [(e)] F_{B7} from fitting an elliptical Gaussian. The best fit Gaussian full-width-at-half-maximum along major and minor axis are given in the format BMAJ×BMIN. [(f)] Non-detection, we report the intensity at the expected position of PDS 70c. [(g)] An elliptical Gaussian fit is not possible because the source is confused with the bright ring.

Appendix C: Gridded *uv*-plane time-differential photometry

The photometric extraction of the variable signal can also be measured in gridded visibility data. We can compute the gridded visibilities, in natural weights, for both the concatenated dataset, $\tilde{V}_{\rm conc}$, with weights $W_{\rm conc}$, and in each individual EB, $\tilde{V}_{\rm EB}$, with weights $W_{\rm EB}$. In an extension of the scheme used in the `visalign` package (Casassus & Cárcamo 2022), the residuals are

$$\tilde{V}_{\rm diff} = \tilde{V}_{\rm EB} - \tilde{V}_{\rm conc} \tag{C.1}$$

with weights

$$W_{\rm diff} = \frac{W_{\rm conc} \times W_{\rm EB}}{W_{\rm conc} + W_{\rm EB}}. \tag{C.2}$$

Such weights naturally match the *uv* sampling functions of both datasets in comparison.

The dirty images of the variable signal in each EB can be used as a consistency test between the photometry in the raw and gridded approaches. The point-source flux density in Eq. 1 is a function of position, and can also be viewed as the dirty map of the residual visibilities corrected for primary-beam attenuation. In the gridded approach, the dirty map is

$$I_{\rm diff}(\boldsymbol{x}) = \frac{\sum_{i,j}^{N} W_{\rm diff}(\boldsymbol{u}_{i,j})\, \tilde{V}_{\rm diff}(\boldsymbol{u}_{i,j})\, e^{-2\pi i \boldsymbol{u}_{i,j}\cdot\boldsymbol{x}}}{\sum_{i,j}^{N} W_{\rm diff}(\boldsymbol{u}_{i,j})}, \tag{C.3}$$

in units of Jy beam^{-1}, and for a grid of side N.

Fig. B.1 compares the dirty maps of the best visibility residuals, i.e. after both alignment and self-calibration, for both approaches. The row labelled '`visalign`, apcal' refers to the dirty maps of the raw residuals, after subtraction of the model visibilities that fit the concatenated dataset, while the row labelled 'gridded' refers to the direct subtraction of the concatenated dataset, i.e. $\tilde{V}_{\rm diff}$. Both version yield similar images, with differences below the noise level, which satisfies this consistency test.

Appendix D: Application to deep Band 7 data

We applied differential photometry to the LB19 Band 7 dataset (Benisty et al. 2021), which was acquired in 3 EBs, two from 27/7/2019, and one from 30/7/2019, and each ∼ 1h15m long. Differential photometry yields the residual flux densities ΔF_{B7} shown in Fig. D.1, where no variability can be picked up among the three EBs.

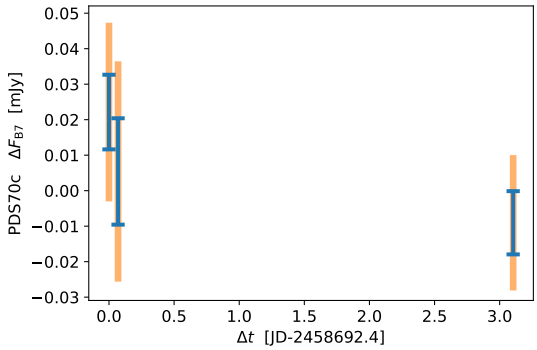

Fig. D.1. Same as Fig. 2, but for the LB19 dataset. The blue error bars stem from the original visibility weights (in this case without the application of `statwt`), while the orange bars stem from the spatial scatter.

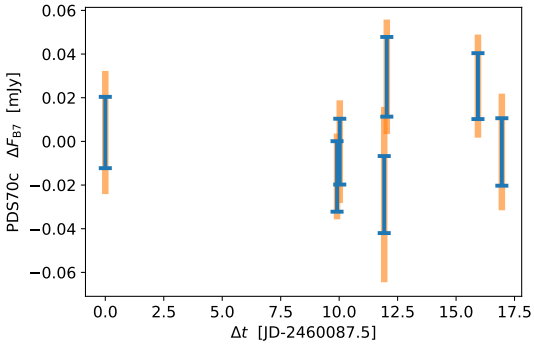

Fig. D.2. Same as Fig. 2, but for the IB23 dataset (2023 Band 7 observations).

We also revisited the full reduction and alignment of the IB23 dataset, and applied time-differential photometry for each EB, as shown in Fig. D.2. The weighted-average residual flux density is $\Delta F_{B7} = 0.2 \pm 8\,\mu$Jy, with a weighted scatter of $18\,\mu$Jy, which represents ∼15% of the flux density reported by (Domínguez-Jamett et al. 2025, of $121 \pm 13\,\mu$Jy). The reduced χ^2 is 0.6 (with 6 degrees of freedom), and consistent with a constant distribution. We therefore reach the same conclusion as Domínguez-Jamett et al. (2025), in the sense that the observed scatter stems purely from the thermal uncertainties (which appear to be somewhat conservative).

In an attempt to pick-up fine-grained variability, we split the seven EBs from IB23 in six equal intervals, each ∼20 min long, and aligned the resulting 'sub-EBs' using `VisAlign`. The reference EB was chosen as 2/6/2023, as it was acquired under

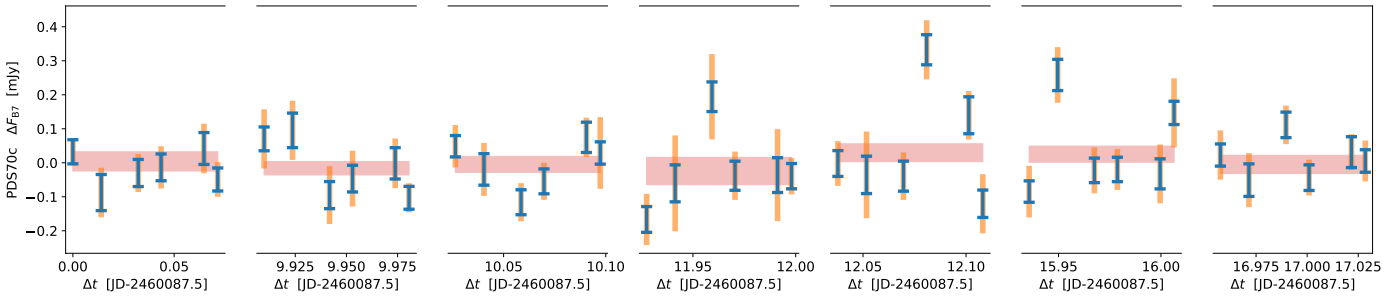

Fig. D.3. Same as Fig. 2, but for the fine-grained IB23 dataset, splitting each EB into 6 intervals. The blue error bars stem from the `statwt` visibility weights, while the orange bars stem from the spatial scatter. The coarser measurements shown in transparent red boxes, with total vertical extension of 2σ, are reproduced from Fig. D.2, and correspond to extractions over the full EB.

the best conditions. The corrections in flux scales were all less than 2%, and the pointing corrections less than 16 mas, which reflects the excellent weather. We then concatenated the aligned sub-EBs for joint imaging, and applied differential photometry (i.e. we used the residuals for the photometry of PDS 70c in the *uv*-plane).

The fine-grained measurements of $\Delta F_{\rm B7}$ shown in Fig. D.3 seem to be indicative of variability, as the reduced χ^2 is 1.67 (with 41 degrees of freedom). This corresponds to a detection of variability at 99.6% confidence, or 2.62 σ. The weighted scatter is $\sigma_s = 13 \pm 2\,\mu$Jy, with bootstrapped uncertainties. The intrinsic variability of PDS 70c, $\sigma_{\rm int}$, can be estimated as an additional source of noise, added in quadrature to each measurement of $\Delta F_{\rm B7}(t)$, such that the reduced χ^2 of the PDS 70c time-series is brought down to unity. In this case we find $\sigma_{\rm int} = 59 \pm 25\,\mu$Jy, with bootstrapped uncertainties. Fixing $F_{\rm B7}$ to the value for IB23 in Table 1, this scatter corresponds to 49% ± 21%.

However, the limitations on self-calibration discussed in Sect. B suggest that the rapidly varying antenna gains represent a source of systematic noise that cannot be corrected through alignment to a global flux scale with `VisAlign`. Also, such non-thermal residuals would not be accounted for in the spatial scatter along the orbit of PDS 70c, since that region is approximately devoid of signal. A test on synthetic and constant point sources is required, with the same flux density as PDS 70c, and at the positions described in Sect. 2. These three control point-sources have $\Delta F_{\rm B7}(t)$ time series which result in reduced χ^2 values of 1.35, 1.29 and 1.36, which are all consistent with a constant value (the corresponding significance of a non-constant value is $\sim 1.4\sigma$).